

# **Exploration of spatio-temporal correlation between AOD and precipitation rates in the Aral Sea Basin based on partial correlations**

## **Seminar on Climate Change and Precipitation**

Faculty of Geography, University of Marburg

Sarah Brüning

Darius A. Görgen

### **Lecturer**

Dr. Boris Thies

### **Date**

April 30, 2020

### **Number of words**

4000

# Contents

<b>Contents</b> . . . . .	i
<b>List of Figures</b> . . . . .	ii
<b>1 Introduction</b> . . . . .	1
<b>2 Data and Methods</b> . . . . .	2
2.1 Study area . . . . .	2
2.2 Satellite products . . . . .	3
2.2.1 Precipitation . . . . .	4
2.2.2 Relative Humidity . . . . .	4
2.3 Methodology . . . . .	4
<b>3 Results</b> . . . . .	6
3.1 Temporal and spatial variations of P and RH . . . . .	6
3.2 Correlation analysis between AOD and P . . . . .	10
<b>4 Discussion</b> . . . . .	16
<b>5 Conclusion</b> . . . . .	16
<b>6 References</b> . . . . .	16

## List of Figures

1	Overview of the study domain within the ASB (Grey-scale values represent elevation, solid red lines national boundaries and dashed isolines average yearly sums of precipitation based on CHIRPS for the years 2003-2018). . . . .	3
2	Boxplots for yearly sum of precipitation [mm]. . . . .	6
3	Boxplots for monthly sums of precipitation [mm]. . . . .	7
4	Spatial distribution of seasonal means for P for MAM (a), JJA (b), SON (c), and DJF (d). .	7
5	Boxplots for yearly median of relative humidity [%]. . . . .	8
6	Boxplots for monthly median relative humidity [%]. . . . .	9
7	Spatial distribution of seasonal means for RH for MAM (a), JJA (b), SON (c), and DJF (d). .	10
8	Spatial distribution of correlation coefficient rho between AOD and P for MAM (a), JJA (b), SON (c), and DJF (d). . . . .	11
9	Spatial distribution of correlation coefficient rho between AOD and P controlled for CER for MAM (a), JJA (b), SON (c), and DJF (d). . . . .	12
10	Spatial distribution of correlation coefficient rho between AOD and P controlled for COT for MAM (a), JJA (b), SON (c), and DJF (d). . . . .	13
11	Spatial distribution of correlation coefficient rho between AOD and P controlled for CWP for MAM (a), JJA (b), SON (c), and DJF (d). . . . .	13
12	Spatial distribution of correlation coefficient rho between AOD and P controlled for RH for MAM (a), JJA (b), SON (c), and DJF (d). . . . .	14
13	Spatial distribution of correlation coefficient rho between AOD and P controlled for all other variables for MAM (a), JJA (b), SON (c), and DJF (d). . . . .	15
14	Correlation coefficients for all pixels with significant correlations by season. . . . .	16

# 1 Introduction

In the last years, an increasing scientific interest has been awoken in terms of the interaction between aerosols and the elements of the hydrological cycle (Ng et al., 2017, p. 1). Precipitation patterns and their influence on human's living environment can be connected with a variety of ecological, economic and social challenges on different spatial extents (Boucher et al., 2013, p. 573 ff.). Especially in semi-arid and arid regions changes in rainfall rates can affect health of local residents (Issanova et al., 2015, p. 3213ff.). Where water is an already scarce resource, further decreases will promote rising vulnerability to external threats (*ibid.*). Regarding this, the Aral Sea region can be seen as a first-class example for investigations between aerosols and rainfall activities (Shen et al., 2019, p. 1). With the desertification of the Aral Sea it has been subject to substantial changes in terms of water availability (Groll et al., 2019, p. 1). Deserts contain a high proportion of mineral aerosols, which may initiate climatological mechanisms of high complexity and, ultimately, a shift in precipitation rates (Boucher et al., 2013, p. 573 ff.). Still, it is hard to quantify the effects on other environmental parameters (Ng et al., 2017, p. 1). The relationship between aerosols and cloud microphysics as well as precipitation patterns remains one of the biggest uncertainties in climate studies (Altaratz et al., 2013, p. 1). Aerosols play a major role in changes of the earth's energy budget (Ng et al., 2017, p. 1) and can be seen as an important component of global climate (Carrico et al., 2003, p. 1). There exist four major terrestrial sources for atmospheric aerosols which, based on their chemical composition, either absorb or scatter incoming solar and terrestrial radiation (Sharif et al., 2015, p. 657f). These direct effects may cool the surface and affect evaporation (Ng et al., 2017, p. 1). Also, aerosols act as cloud condensation nuclei (CCN) leading to more and smaller droplets, which is called the first indirect aerosol effect (Costantino and Bréon, 2010, p. 1). The result is a suppression of precipitation, while the second indirect effect prolongs the cloud's lifetime through the prevention of coalescence favouring the occurrence of extreme events (Ng et al., 2017, p. 2). By heating the cloud, the coverage area is reduced, again leading to a higher amount of radiation on the ground. This attenuates surface evaporation and further decreases rainfall (*ibid.*). A number of studies showed the presence of a strong seasonality in regard to aerosol concentration in Central Asia (Ge et al., 2016, p. 62ff.; Li and Sokolik, 2018, p. 2ff.). The highest values occur in spring while the lowest concentrations have been measured in winter (*ibid.*). However, some studies suggest the indicated perturbation of the hydrological cycle to be more distinct in some places than in others (Ng et al., 2017, p. 2). The goal of this study is to analyse temporal and spatial variations of aerosols in the Aral Sea region in relation to precipitation patterns. Following a prior seminar work regarding the analysis of aerosol and cloud microphysical properties, it continues striving for an adequate estimation of the relationship between hydro-climatological parameters. Therefore, the analysis consists of the investigation of potential trends,

their strength and direction in regard to aerosol concentration to rainfall rates. In order to display the overall effects, cloud microphysical parameters will be included as well as the atmosphere's relative humidity because of its critical role on rainfall variability (Altaratz et al., 2013, p. 1f.; Carrico et al., 2003, p. 2). Some studies suggest high rain rates to be associated with a rising aerosol concentration (Boucher et al., 2013, p. 4). Otherwise, contrary results have been observed as well (Ng et al., 2017, p. 1ff.). In general, time and space seem to be crucial (Grandey et al., 2014, p. 5678ff.). The hygroscopicity of aerosols cause the relative humidity to be one of the most important drivers for the observed relationship between AOD and rainfall (Ng et al., 2017, p. 2f.). When it reaches a certain concentration, it can alter the results of correlation analyses mainly through two effects (Altaratz et al., 2013, p. 1f.). First, relative humidity may cause, depending on the aerosols' chemical properties, substantial growth of the particles in an humid environment (Carrico et al., 2003, p. 1), leading to coalescence of the droplets (Ng et al., 2017, p. 2ff.). This depicts a rather positive relation between the variables (Grandey et al., 2014, p. 5678). Second, wet scavenging of aerosols through rainfall can occur in a mostly convective environment (Grandey et al., 2014, p. 5680ff.). It acts as an aerosol sink and results in a negative relationship between the aerosol concentration and precipitation or rather relative humidity (*ibid.*). Consequently, a negative correlation may not only reflect suppressed precipitation (Ng et al., 2017, p. 9). Both effects demonstrate the importance of the atmospheres' humidity in questions of aerosol-precipitation relationships and thus will be evaluated in the following study.

## 2 Data and Methods

### 2.1 Study area

The Aral Sea basin is located in the border region between Kazakhstan and Uzbekistan (57 – 67 °E, 42 – 49 °N) and acts as the tail-end lake of the contributing rivers Amu Darya and Syr Darya (Fig. 1). The study area is part of the global dust belt and shows typical features of a temperate continental climate with semi-arid to arid conditions. The summers are short and hot with a mean of 28.2 °C while winters are long and cold with a mean of -3.6 °C. Precipitation rates are quite low with a mean of about 82.1 *mm/year* and a maximum during winter (Gaynullaev et al., 2012, p. 287). Strong winds are often to be recorded in the study area (Issanova et al., 2015, p. 3213f.). The Aral Sea once has been the fourth largest lake on earth covering a water volume of 1.093 *km*<sup>3</sup> in 1960 (Gaynullaev et al., 2012, p. 286). Since then, it has been gradually shrinking due to over-exploitation of its natural resources by water abstraction for irrigation agriculture as well as the impacts of climate change (Ge et al., 2016, p. 2; Shen et al., 2019, p. 2031). In the year 2003,

it finally split into eastern and western parts. The exposed lake bed consists of salt soils and loose sand dunes turning the former southern and western part of the lake into the Aralkum desert (Shen et al., 2019, p. 2031f., 2016, p. 624) which comprises of  $57.500 \text{ km}^2$  (Opp et al., 2019, p. 3). The landscape is characterized by frequent salt and sand dust storms which may bear several threats to the ecosystem and local human's health (Ge et al., 2016, p. 4). It has been stated that the spatial and temporal dust deposition variability is highly significant (Opp et al., 2019, p. 1ff.).

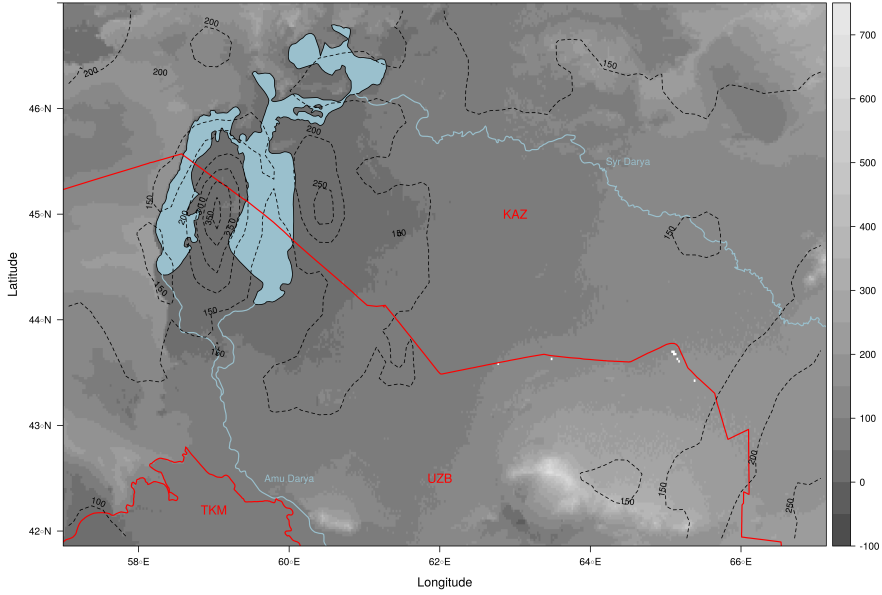


Figure 1: Overview of the study domain within the ASB (Grey-scale values represent elevation, solid red lines national boundaries and dashed isolines average yearly sums of precipitation based on CHIRPS for the years 2003-2018).

## 2.2 Satellite products

MODIS (Moderate Resolution Imaging Spectroradiometer) data currently is collected by two platforms (TERRA and AQUA) orbiting the Earth on a Sun-synchronous polar orbit. It measures solar and thermal radiation in 36 bands in resolutions ranging from  $250 \text{ m}$  to  $1 \text{ km}$ . For this study, daily resolution Level-2 data were used for aerosol (MOD/MYD04) (Levy et al., 2017) and cloud (MOD/MYD06) (Platnick et al., 2017) parameters as well as the corresponding geolocation files (MOD/MYD03) (*MODIS Geolocation Fields 5-Min L1A Swath 1km V006*, 2012). For the explanation of the parameter retrieval, the reader is referred to the prior seminar work, as these explanations are not duplicated here, except for the newly included parameters of precipitation and relative humidity.

### **2.2.1 Precipitation**

*Precipitation (P):* Monthly sums of precipitation are derived from the CHIRPS data set. This data set is established by taking long-term monthly average data from ground stations in conjunction with observations from five satellite missions to establish a local regression model with a moving window for each grid cell of  $0.05^{\circ}$  in size (Funk et al., 2015, p. 3f.). The independent variables in the local regressions consist always of the longitude and latitude information as well as one to three additional variables representing either the local elevation, the slope or satellite observations. Potential residuals in comparison to the FAO climate normals are interpolated using inverse distance weighting and are than added to the local estimates (Funk et al., 2015, p. 3). In a last step, for every pixel the five nearest ground stations are used to apply another inverse distance weighting algorithm. Here, an estimate of the decor-relation slope from the predicted precipitation and the observed precipitation at the neighboring stations are used to calculated a weighted average (Funk et al., 2015, p. 3).

### **2.2.2 Relative Humidity**

*Relative Humidity (RH):* RH is retrieved using the ERA-5 reanalysis data set processed by the European Centre for Medium-Range Weather Forecasts (ECMWF) (Forecasts, 2017). This data set combines observations and model predictions to get a comprehensive model of global atmospheric conditions at small time steps and a nominal resolution of 31km at the ground, however the data has been regredded to  $0.25^{\circ}$ . The atmosphere is modeled in 137 vertical levels from the surface to 1 Pa. Here, we used the monthly aggregates of RH only for the first seven atmospheric layers (1000 hPa - 850 hPa) since the other data sets were also summarized to monthly aggregates. 850 Pa was considered an appropriate height level, since local aerosol transports in the region are merely reported to be found above 5 km in height (Chen et al., 2013).

## **2.3 Methodology**

AOD and the cloud parameters were extracted from the respective MODIS data sets using the HEG-Tool (HDF-EOS To GeoTIFF Conversion Tool). It enables a selection of the cloud and aerosol properties clipping the data directly to the area of interest which is leaned on the shape of the study area used by (Ge et al., 2016). The cloud parameters (at 6km nominal resolution) were resampled to the 10km nominal resolution of the AOD data set. The observations of single MODIS overflights were then aggregated to a monthly temporal-resolution, and means were calculated for four different seasons (Spring: March, April, May (MAM);

Summer: June, July, August (JJA); Autumn: September, October, November (SON); Winter: December, January, February (DJJ)) for every year between 2003 to 2018.

The CHIRPS data set already represents monthly aggregates. The cell values were resampled to the 10km resolution of the MODIS data and seasonal aggregates were calculated as described above. For RH, the process was basically identical, except that the median was calculated across the seven vertical layers, before the data was resampled to the same resolution as the other data sets.

To retrieve the correlation between AOD and P and to generate insights to the underlying processes we conduct a number of correlation analysis between these two parameters, while eliminating the influence of cloud parameters and RH. For this approach, we firstly checked if the data fulfills the assumptions to calculate Pearson's correlation. All variables are continuous in form. Pearson's correlation additionally is sensitive for outliers. Similarly to other studies we thus excluded exceptional high AOD values above 0.3. Also, we assume linear relationships between the variables for values below the AOD threshold of 0.3. We then calculated the correlation coefficient between AOD and P while controlling for any other variable. This is achieved by calculating the partial correlation. Partial correlation is used as a measure of the linear dependence between two variables while controlling for the influences of a third. In fact, not the original values of AOD and P are fitted, but rather the residuals which were calculated by using the control variable as a predictor. Thus, only the proportion of variance which cannot be explained by the control variable is subject to the correlation analysis (Salkind, 2010). This approach has been chosen by a number of recent studies investigating relationships between aerosols and cloud microphysics as well as precipitations and seems reasonable to achieve both, investigating the “true” relationship between AOD and P in a complex field of intervening processes and effects and to deliver indications for the dominant processes driving this relationship (Engström and Ekman, 2010; Gryspeerdt et al., 2014; Ng et al., 2017).

The results of this analysis are presented on a pixel basis for each season to display spatial and temporal differences. Additionally, the correlation of all pixels which show a significant relationship at the 95% confidence interval is calculated to investigate the overall direction and strength of correlation between aerosol and cloud parameters (Alam et al., 2010, p. 1170f.).

### 3 Results

#### 3.1 Temporal and spatial variations of P and RH

The temporal and spatial variations of several aerosol and cloud parameters have been presented in the previous seminar paper. Here, we only represent the additional parameters P and RH.

*Temporal and spatial dynamics for P* During the time series under study (2003 - 2018) we can observe a varying pattern for precipitation (Fig. 2). In 2003 we observe relatively high precipitation rates with an average above 200 mm per pixel and a median even slightly higher than the mean, which is in accordance with another study reporting 2003 as a very-wet year in Central Asia (Xu et al., 2016). This amount of high precipitation rates from the year 2003 is not reached again during the time series, instead most of the years indicate a mean value of precipitation below 150 mm per pixel. The years 2008, 2011, and 2014 show exceptional low precipitation, which are note completely in line with the findings of Xu et al. (2016), indicating 2006, 2008 and 2011 as severe drought years. In 2015 and 2016 precipitation is higher than during the other years, however the high precipitation rate of 2003 is not reached.

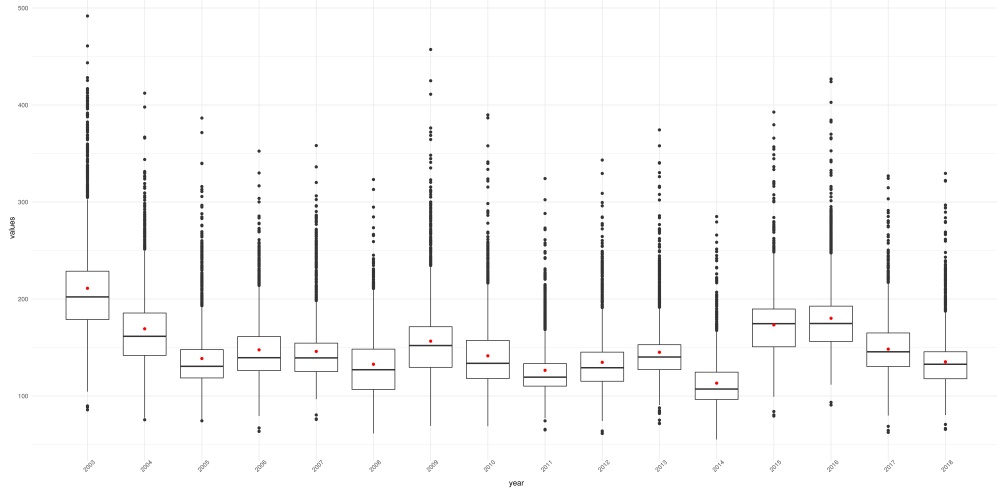


Figure 2: Boxplots for yearly sum of precipitation [mm].

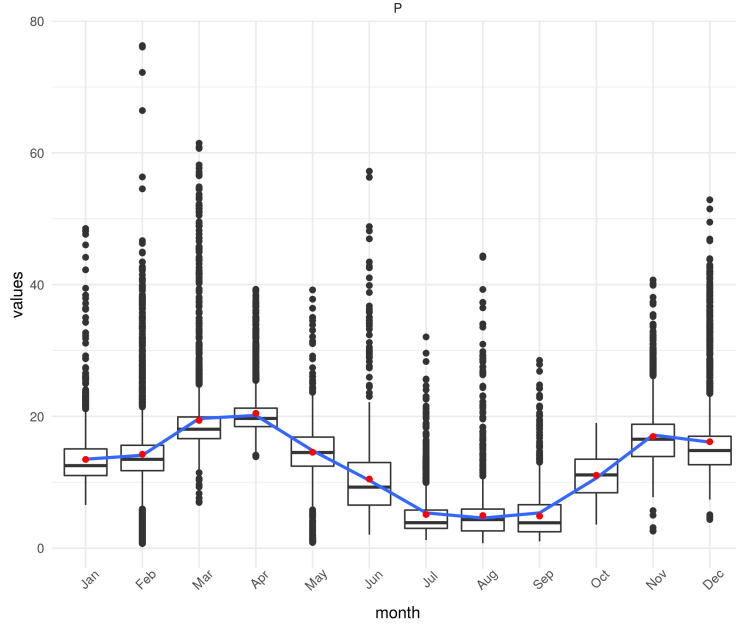


Figure 3: Boxplots for monthly sums of precipitation [mm].

Concerning the intra-annual pattern of precipitation, we observe the highest rates in March and April as well as another peak during November and December of about 19 mm per pixel (Fig. 3). During the summer months of July to September we observe the lowest precipitation rates with means about 5 mm. The seasonality of precipitation is thus clearly visible and is in accordance with the seasonal division we chose here for our analysis.

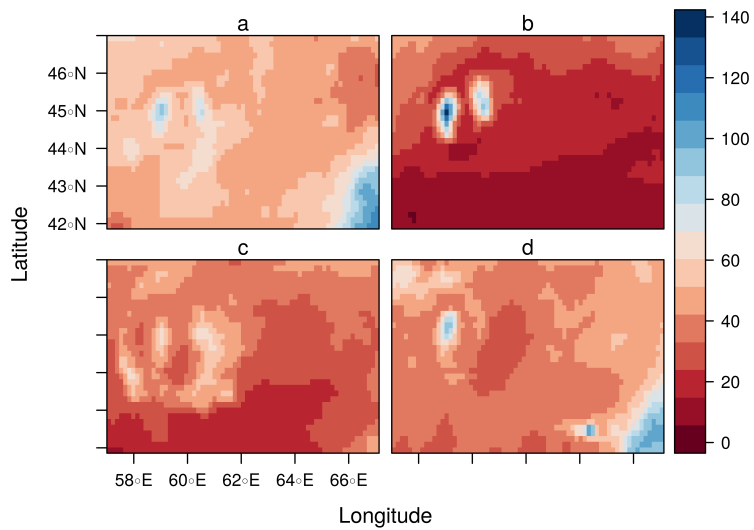


Figure 4: Spatial distribution of seasonal means for P for MAM (a), JJA (b), SON (c), and DJF (d).

The spatial pattern of P shows that higher precipitation rates are found above the Aral Sea and Aralkum dessert (Fig. 4) as well as in the South-East of the study area during the first and fourth season. The second and third season are characterized by very low precipitation rates, especially in the South of the study area. The linear trend analysis indicates significant linear trends only during the first season in the South-East of the study area. Here, moderate to high negative slopes seem to dominate the trend (about -2 to -5 mm/year). During the second season we also observe moderate to high decrease of precipitation rate close to the Aral Sea and its Northern neighborhood. During the third and fourth season we barely observe patterns of significant linear trends.

*Temporal and spatial dynamics for RH* Concerning the inter-annual dynamic of relative humidity, we observe a general decrease of RH per pixel during the first few years (Fig. 5). Similar to P, the highest level of RH is reached in 2003 with a mean value of 50%. In 2010 and 2014, we observe RH values below 40%, and in 2012 and 2018 RH reaches only about 42%. With the exception of 2014, we do not see the gravity of the drought years of 2008 and 2011 in the dynamic of RH. During most other years RH usually reaches between 43 - 46%, however, in 2015 and 2016 the mean is about 48%, in the same years we also observed relatively high precipitation rates.

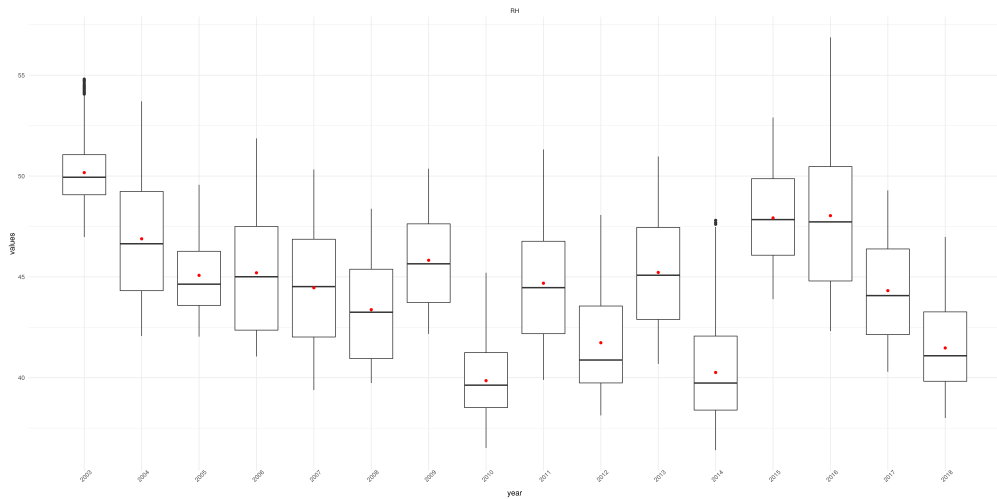


Figure 5: Boxplots for yearly median of relative humidity [%].

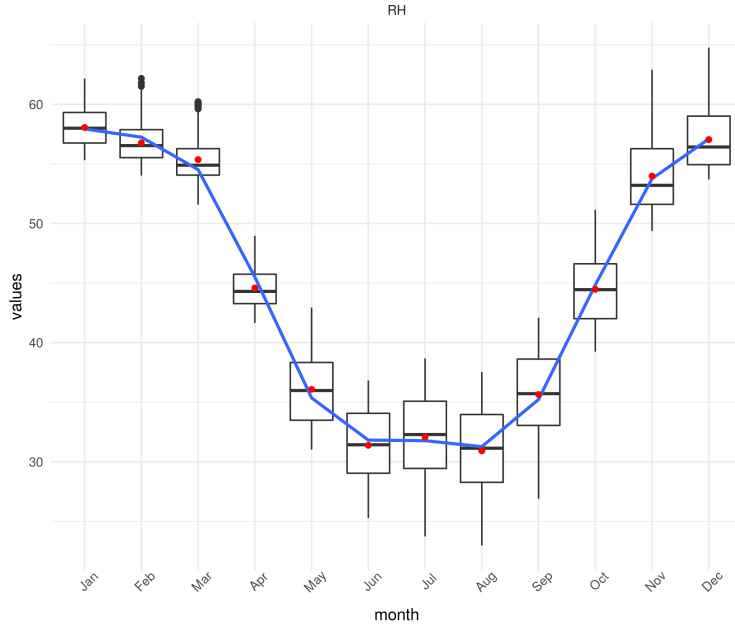


Figure 6: Boxplots for monthly median relative humidity [%].

The intra-annual dynamic of RH follows a very clear seasonal pattern with the lowest RH (~31%) found in the warm summer months June to August (Fig. 6). RH is maximized during December to March, with levels between 55 - 58%. The spatial pattern of RH shows higher values through the study area for the first and fourth season (Fig. 7). For the second and fourth season, the pattern is very similar with the lowest RH found in the South-East and a positive gradient towards the North-West of the study area. However, the values during the second season are substantially lower than compared to the third. Significant linear trends are only found during the second season South of the Aral Sea. Here, low negative slopes dominate the trend (about -0.3%/year).

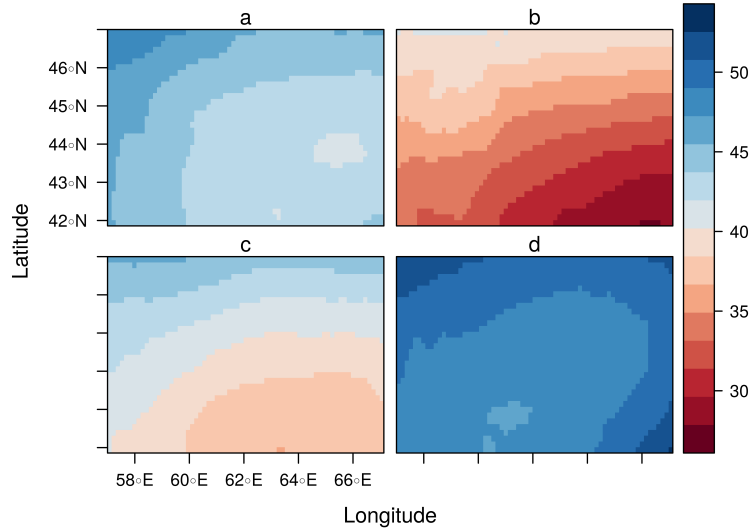


Figure 7: Spatial distribution of seasonal means for RH for MAM (a), JJA (b), SON (c), and DJF (d).

### 3.2 Correlation analysis between AOD and P

As indicated in the methods section, we analysed the partial correlation between AOD and P controlling for three parameters of cloud microphysics and RH. As a baseline we also calculated the correlation without any controlling variable. We excluded all pixels for which there were no observations in AOD at any time step in order to capture the complete time series of the remaining pixels. This areas are indicated in grey color in the figures below.

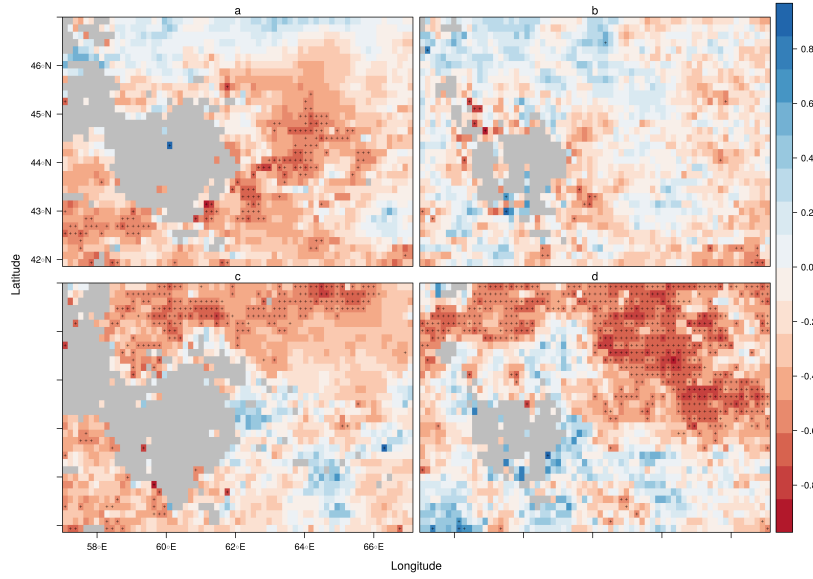


Figure 8: Spatial distribution of correlation coefficient rho between AOD and P for MAM (a), JJA (b), SON (c), and DJF (d).

*Baseline correlation:* Areas with missing values are concentrated around the Aral Sea for all seasons (Fig. 8). During the first and third season, the number of missing observations is higher than during the other seasons. For the first season, we observe a pattern of strongly negative correlation in the center of the study area and South of the Aral Sea. We also observe some, though non-significant, positive correlations in the North and the far South-East of the study area. During the second season, there are only very few locations with significant correlations. In general, the picture is very patchy with positive and negative correlations distributed fairly random in the study area, especially next to the Aral Sea. In the third season we observe a comprehensive patch of negative correlations in the North of the study area and positive correlations in the South. However, the positive correlations are not significant. A similar pattern, though larger in size extending to the South is observed during the fourth season. These correlations are significant and negative and generally between -0.4 and -0.7.

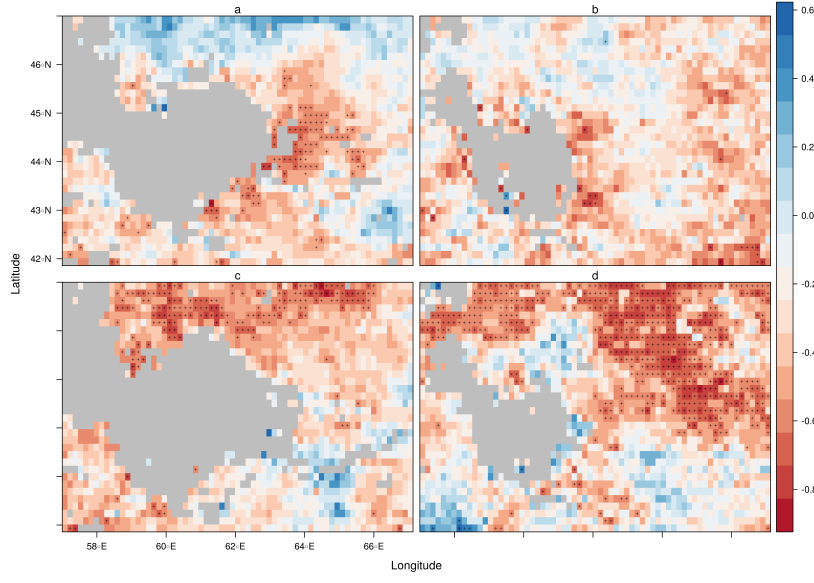


Figure 9: Spatial distribution of correlation coefficient  $\rho$  between AOD and P controlled for CER for MAM (a), JJA (b), SON (c), and DJF (d).

#### *Partial Correlation controlling for CER*

Concerning the spatial distribution of the correlations, the pattern is very similar to the baseline correlation analysis (Fig. 9). However, we observe slight increases in the amplitude of the significant negative correlations for the seasons (between -0.6 and -0.85).

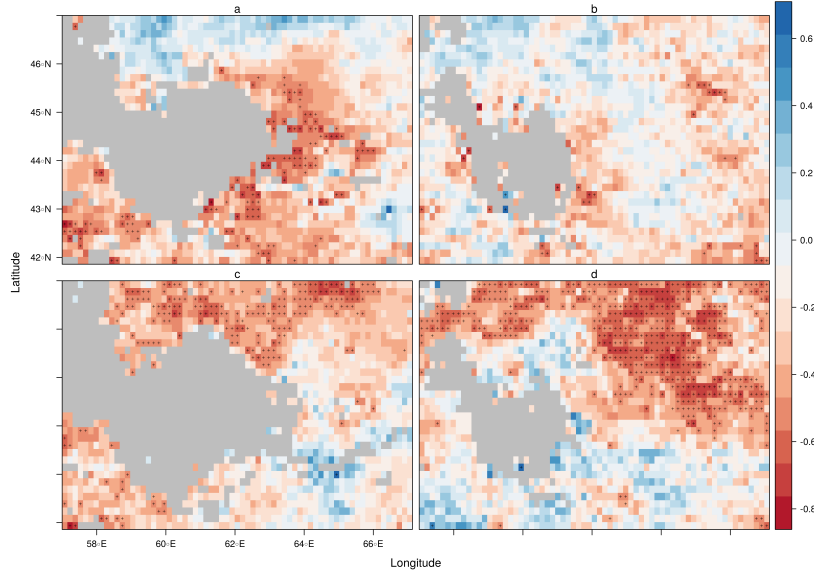


Figure 10: Spatial distribution of correlation coefficient rho between AOD and P controlled for COT for MAM (a), JJA (b), SON (c), and DJF (d).

*Partial Correlation controlling for COT:* The amplitude and spatial distribution is very similar to the preceding correlation analysis (Fig. 10). However, for the third and fourth season the total number of significant correlations decreases and the comprehensive areas of negative correlations are observed to become more patchy.

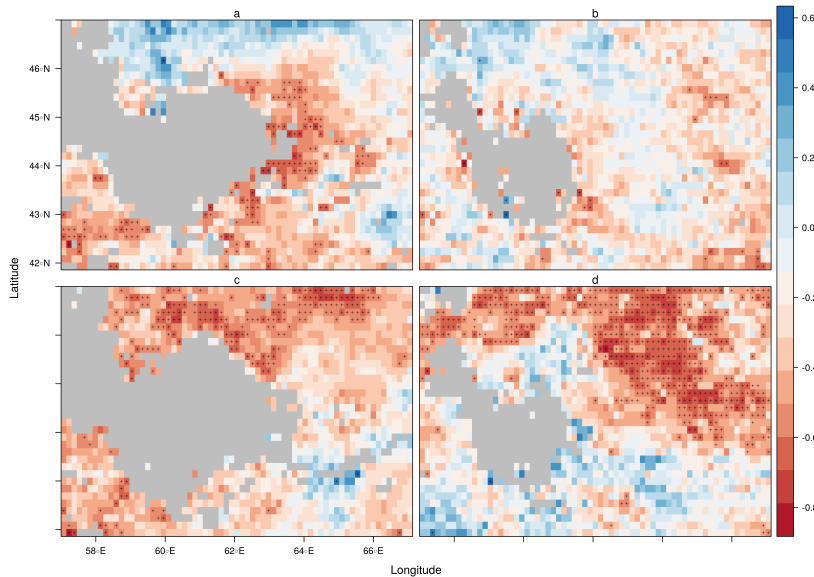


Figure 11: Spatial distribution of correlation coefficient rho between AOD and P controlled for CWP for MAM (a), JJA (b), SON (c), and DJF (d).

### *Partial Correlation controlling for CWP*

For CWP again, the main patterns compared to the other analysis do not change (Fig. 11). However, there seems to be a slight increase in the negative correlations during the fourth season.

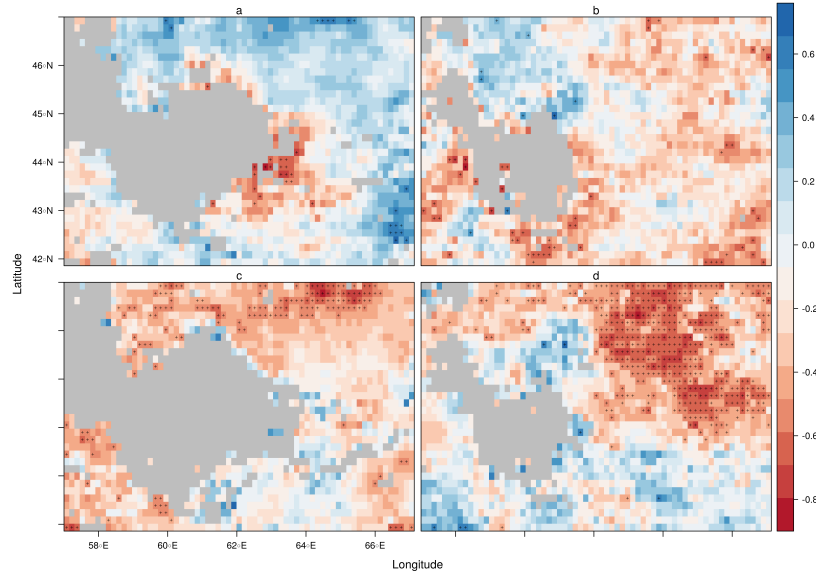


Figure 12: Spatial distribution of correlation coefficient rho between AOD and P controlled for RH for MAM (a), JJA (b), SON (c), and DJF (d).

*Partial Correlation controlling for RH:* When controlling for RH, some changes can be observed (Fig. 12). In the first season, the size of the patch of significant negative correlations around the Aral Sea and Aralkum dessert is substantially reduced. The same finding holds true for the Northern patch of negative correlations in the third season. In the fourth season, directly North of the Aral Sea, we observe fewer significant negative correlations, however, the comprehensive patch in the Center of the study area can still be observed. In general, when controlling for RH, there seems to be a shift into the direction of positive correlations, because the positive correlations increase in amplitude without reaching the level of significance.

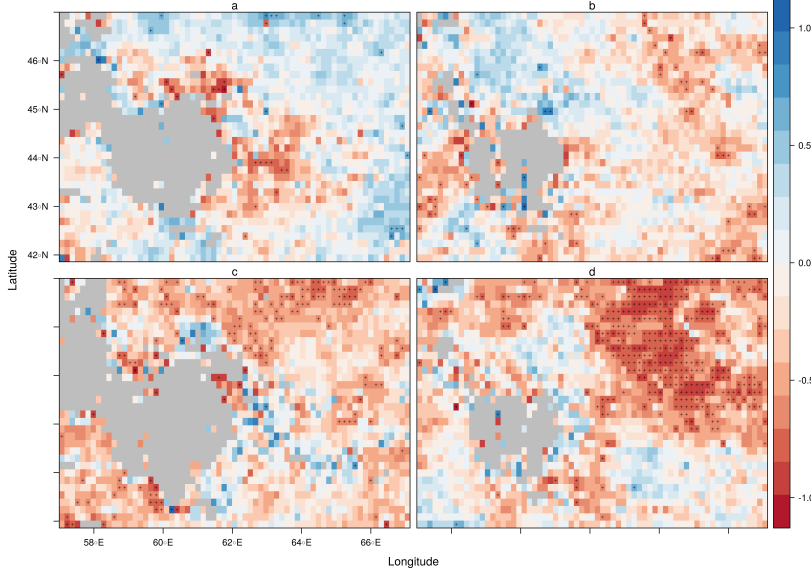


Figure 13: Spatial distribution of correlation coefficient rho between AOD and P controlled for all other variables for MAM (a), JJA (b), SON (c), and DJF (d).

*Partial Correlation controlling for CWP, COT, CWP, and RH:* When controlling for all variables, the correlations patterns get more patchy for every season, which means that in large proportions of the study area we observe non-significant positive and negative correlations in fairly random patterns next to each other (Fig. 13). The exceptions are a comprehensive patch of negative correlations in the North of the study area in the third season, though its size is substantially reduced compared to the baseline analysis, as well as the comprehensive patch of negative correlations in the Center of the study area during the fourth season. Compared to the analysis controlling for RH only, the non-significant positive correlations also seem to decrease in amplitude.

*Analysis of significant correlations:* Figure 14 shows the correlations of selected pixels which showed significant correlations for all four seasons and based on the controlling scenario. For all seasons and analysis we observe negative correlations between AOD and P between -0.1 and -0.38. The correlation values for the second season are substantially closer to 0 than compared to all other seasons which can be easily explained by the very small number of pixels which showed significant correlations during this seasons and the general very low precipitation rates during this season. For the first and third season, controlling for parameters of cloud microphysics seem to increase the negative correlations compared to the baseline analysis while controlling for RH delivers smaller correlations values. This observations does not hold for the fourth season, where controlling for RH increases the correlation coefficient, while controlling for cloud microphysics shows little to no effects. When all variables are controlled for, we observe no effects on the correlation coefficient for the

first and fourth season. In the third season, controlling for all variables decreases the coefficient from -0.38 to -0.28.

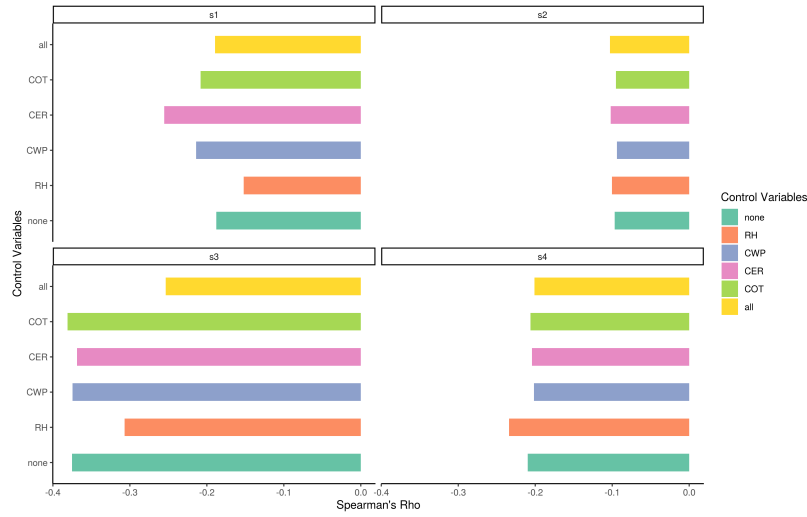


Figure 14: Correlation coefficients for all pixels with significant correlations by season.

## 4 Discussion

## 5 Conclusion

## 6 References

Alam, K., Iqbal, M.J., Blaschke, T., Qureshi, S., Khan, G., 2010. Monitoring spatio-temporal variations in aerosols and aerosol-cloud interactions over Pakistan using MODIS data. *Advances in Space Research* 46, 1162–1176. <https://doi.org/10.1016/j.asr.2010.06.025>

Altaratz, O., Bar-Or, R.Z., Wollner, U., Koren, I., 2013. Relative humidity and its effect on aerosol optical depth in the vicinity of convective clouds. *Environmental Research Letters* 8. <https://doi.org/10.1088/1748-9326/8/3/034025>

Boucher, O., Randall, D., Artaxo, P., Bretherton, C., Feingold, G., Forster, P., Kerminen, V.-M., Kondo, Y., Liao, H., Lohmann, U., Rasch, P., Satheesh, S., Sherwood, S., Stevens, B., Zhang, X., 2013. Clouds and Aerosols, in: Stocker, T., Qin, D., Plattner, G.-K., Tignor, M., Allen, S., Boschung, J., Nauels, A., Xia, Y., Bex, V., Midgley, P. (Eds.), *Climate Change 2013: The Physical Science Basis. Contribution*

of Working Group I to the Fifth Assessment Report of the Intergovernmental Panel on Climate Change. Cambridge University Press, Cambridge, United Kingdom; New York, NY, USA., pp. 465–657. <https://doi.org/10.1017/CBO9781107415324.015>

Carrico, C.M., Kus, P., Rood, M.J., Quinn, P.K., Bates, T.S., 2003. Mixtures of pollution, dust, sea salt, and volcanic aerosol during ACE-Asia: Radiative properties as a function of relative humidity. *Journal of Geophysical Research D: Atmospheres* 108. <https://doi.org/10.1029/2003jd003405>

Chen, B.B., Sverdlik, L.G., Imashev, S.A., Solomon, P.A., Lantz, J., Schauer, J.J., Shafer, M.M., Artamonova, M.S., Carmichael, G.R., 2013. Lidar Measurements of the Vertical Distribution of Aerosol Optical and Physical Properties over Central Asia. *International Journal of Atmospheric Sciences* 2013, 1–17. <https://doi.org/10.1155/2013/261546>

Costantino, L., Bréon, F.M., 2010. Analysis of aerosol-cloud interaction from multi-sensor satellite observations. *Geophysical Research Letters* 37. <https://doi.org/10.1029/2009GL041828>

Engström, A., Ekman, A.M., 2010. Impact of meteorological factors on the correlation between aerosol optical depth and cloud fraction. *Geophysical Research Letters* 37, 1–4. <https://doi.org/10.1029/2010GL044361>

Forecasts, E.C. for M.-R.W., 2017. ERA5 Reanalysis (0.25 Degree Latitude-Longitude Grid). <https://doi.org/https://doi.org/10.5065/BH6N-5N20>

Funk, C., Peterson, P., Landsfeld, M., Pedreros, D., Verdin, J., Shukla, S., Husak, G., Rowland, J., Harrison, L., Hoell, A., Michaelsen, J., 2015. The climate hazards infrared precipitation with stations - A new environmental record for monitoring extremes. *Scientific Data* 2, 1–21. <https://doi.org/10.1038/sdata.2015.66>

Gaynullaev, B., Chen, S.-C., Gaynullaev, D., 2012. Changes in water volume of the Aral Sea after 1960. *Applied Water Science* 2, 285–291. <https://doi.org/10.1007/s13201-012-0048-z>

Ge, Y., Abuduwaili, J., Ma, L., Liu, D., 2016. Temporal Variability and Potential Diffusion Characteristics of Dust Aerosol Originating from the Aral Sea Basin, Central Asia. *Water, Air, and Soil Pollution* 227. <https://doi.org/10.1007/s11270-016-2758-6>

Grandey, B.S., Gururaj, A., Stier, P., Wagner, T.M., 2014. Rainfall-aerosol relationships explained by wet scavenging and humidity. *Geophysical Research Letters* 41, 5678–5684. <https://doi.org/10.1002/2014GL060958>

Groll, M., Opp, C., Issanova, G., Vereshagina, N., Semenov, O., 2019. Physical and Chemical Characterization of Dust Deposited in the Turan Lowland (Central Asia). *E3S Web of Conferences* 99, 03005. <https://doi.org/10.1051/e3sconf/20199903005>

- Gryspeerdt, E., Stier, P., Grandey, B.S., 2014. Cloud fraction mediates the aerosol optical depth-cloud top height relationship. *Geophysical Research Letters* 41, 3622–3627. <https://doi.org/10.1002/2014GL059524>
- Issanova, G., Abuduwaili, J., Galayeva, O., Semenov, O., Bazarbayeva, T., 2015. Aeolian transportation of sand and dust in the Aral Sea region. *International Journal of Environmental Science and Technology* 12, 3213–3224. <https://doi.org/10.1007/s13762-015-0753-x>
- Levy, R., Hsu, C., Sayer, A., Mattoo, S., Lee, J., 2017. MODIS Atmosphere L2 Aerosol Product. NASA MODIS Adaptive Processing System, Goddard Space Flight Center. [https://doi.org/10.5067/MODIS/MOD04\\_L2.061;10.5067/MODIS/MYD04\\_L2.061](https://doi.org/10.5067/MODIS/MOD04_L2.061;10.5067/MODIS/MYD04_L2.061)
- Li, L., Sokolik, I.N., 2018. Analysis of dust aerosol retrievals using satellite data in Central Asia. *Atmosphere* 9. <https://doi.org/10.3390/atmos9080288>
- MODIS Geolocation Fields 5-Min L1A Swath 1km V006, 2012.. MODIS Characterization Support Team, Level 1; Atmosphere Archive; Distribution System (LAADS). <https://doi.org/10.5067/MODIS/MOD03.006;10.5067/MODIS/MYD03.006>
- Ng, D.H.L., Li, R., Raghavan, S.V., Liong, S.Y., 2017. Investigating the relationship between Aerosol Optical Depth and Precipitation over Southeast Asia with Relative Humidity as an influencing factor. *Scientific Reports* 7, 1–13. <https://doi.org/10.1038/s41598-017-10858-1>
- Opp, C., Groll, M., Semenov, O., Vereshagina, N., Khamzina, A., 2019. Impact of the Aral Sea Syndrome - the Aralkum as a Man-Made Dust Source. *E3S Web of Conferences* 99, 03003. <https://doi.org/10.1051/e3sconf/20199903003>
- Platnick, S.E., Ackerman, S.A., King, M.D., Meyer, K., Menzel, P., Frey, R., Holz, R., Baum, B., Yang, P., 2017. MODIS atmosphere L2 cloud product (06\_L2). NASA MODIS Adaptive Processing System, Goddard Space Flight Center. [https://doi.org/10.5067/MODIS/MOD06\\_L2.061;10.5067/MODIS/MYD06\\_L2.061](https://doi.org/10.5067/MODIS/MOD06_L2.061;10.5067/MODIS/MYD06_L2.061)
- Salkind, N., 2010. Encyclopedia of Research Design. <https://doi.org/10.4135/9781412961288 NV - 0>
- Sharif, F., Alam, K., Afsar, S., 2015. Spatio-Temporal distribution of aerosol and cloud properties over Sindh using MODIS satellite data and a HYSPLIT model. *Aerosol and Air Quality Research* 15, 657–672. <https://doi.org/10.4209/aaqr.2014.09.0200>
- Shen, H., Abuduwaili, J., Ma, L., Samat, A., 2019. Remote sensing-based land surface change identification and prediction in the Aral Sea bed, Central Asia. *International Journal of Environmental Science and Technology* 16, 2031–2046. <https://doi.org/10.1007/s13762-018-1801-0>

Shen, H., Abuduwalili, J., Samat, A., Ma, L., 2016. A review on the research of modern aeolian dust in Central Asia. Arabian Journal of Geosciences 9. <https://doi.org/10.1007/s12517-016-2646-9>

Xu, H. jie, Wang, X. ping, Zhang, X. xiao, 2016. Decreased vegetation growth in response to summer drought in Central Asia from 2000 to 2012. International Journal of Applied Earth Observation and Geoinformation 52, 390–402. <https://doi.org/10.1016/j.jag.2016.07.010>